Computational Mechanics 26 (2000) 185–196 © Springer-Verlag 2000

Aspects of finite element implementation of critical state models

D. Sheng, S. W. Sloan, H. S. Yu

Abstract In this paper, some practical aspects of the finite element implementation of critical state models are discussed. Improved automatic algorithms for stress integration and load and time stepping are presented. The implementation of two generalized critical state soil models, with one described first in this paper and the other recently published elsewhere, is discussed. The robustness and correctness of the proposed numerical algorithms are illustrated through both coupled and uncoupled analyses of geotechnical problems.

Introduction

The application of plasticity theory in soil mechanics has enjoyed a fruitful history over the last 30 years, with a major milestone being the development of critical state models by Roscoe et al. at the University of Cambridge [1–4]. The original Cam-clay model, due to Roscoe and Schofield [2] and Schofield and Wroth [3], and the modified Cam-clay model, due to Roscoe and Burland [4], are now widely used for predicting soil behavior. In recent times, these classical critical state models have been modified in various ways by many researchers to cover different soil types and loading conditions in an attempt to achieve a better prediction of experimental data [5–13].

The implementation of critical state models in finite element computer programs was first carried out in the early 1970s [14–18]. Since then, a large number of critical state models have been implemented in both commercial and research finite element codes (see, for example, Gens and Potts [19]). In uncoupled analyses, the performance of these numerical models depends on the choice of stress integration and load stepping scheme [20–24] while, for coupled problems, it is necessary to select an appropriate time stepping scheme [25–26]. As pointed out by Gens and Potts [19], critical state models are particularly vulnerable to numerical breakdown and it is not easy to predict which solution procedure will be satisfactory for a particular problem. Robust algorithms that work for a wide variety of soil types and loading conditions are thus urgently needed for accurate finite element computations using critical state models.

This paper presents an accurate and reliable automatic procedure for implementing critical state models that has been developed at the University of Newcastle. Particular attention is focused on the algorithms of Sloan [27] and Abbo [28] for stress integration, Abbo and Sloan [29] for load-displacement integration in uncoupled analysis, and Sloan and Abbo [30] for time integration in coupled analysis. In this paper, these newly developed automatic algorithms have been further refined to better handle the nonlinear elasticity in critical state models. A number of examples are analysed in the paper, and include the modelling of drained and undrained triaxial tests, undrained expansion of a cylindrical cavity, and drained and undrained loading of a rigid footing. Both uncoupled and coupled analyses are used in the calculations.

D. Sheng, S. W. Sloan (✉), H. S. Yu
Department of Civil, Surveying & Environmental Engineering, The University of Newcastle, NSW 2308, Australia

Finite element implementation of critical state models

Normalization of yield function and plastic potential

In critical state models, the yield function and plastic potential are usually expressed in terms of stress invariants. For example, the yield functions for the original Cam-clay model and the modified Cam-clay model are often written as

$$f = q - Mp' \ln(p'_0/p') \tag{1}$$

and

$$f = q^2 - M^2(p'p'_0 - p'^2) \tag{2}$$

where q is the deviator stress, p' is the effective mean stress, M is the slope of the critical state line in a p'–q diagram, and p'_0 is the isotropic preconsolidation pressure (which is also the current location of the yield surface when $q = 0$).

Since the value of the yield function is normally used to determine if a stress state is elastic ($f < 0$) or plastic ($f = 0$), it is appropriate to scale these functions against a stress parameter so that their values are not significantly influenced by the magnitudes of the stresses. In practice, the conditions $f < 0$, $f = 0$ and $f > 0$ are always checked using a specified yield surface tolerance, which is typically in the range 10^{-6}–10^{-12}. For critical state models, a good normalisation parameter is the current isotropic preconsolidation pressure p'_0. When normalized by p'_0, the yield functions (1) and (2) may be rewritten as

$$f = \frac{q}{p'_0} - M\frac{p'}{p'_0}\ln\left(\frac{p'_0}{p'}\right) \tag{3}$$

$$f = \frac{q^2}{p'^2_0} - M^2\left[\frac{p'}{p'_0} - \frac{p'^2}{p'^2_0}\right] \tag{4}$$

Note that the absolute values of the yield functions in (3) and (4) only depend on the relative stresses p'/p'_0 and q/p'_0. Since for plastic loading p'_0 increases (decreases) with increasing (decreasing) p' or increasing (decreasing) q, the accuracy of the yield functions defined by (3) and (4) is obviously less dependent on the stress magnitudes than those defined by (1) and (2). Another advantage of this normalization is that the yield surfaces defined by (3) and (4) are static in the normalized stress plane plot of p'/p'_0 versus q/p'_0.

Tangent and secant elastic modulii

In displacement or displacement-pore pressure based finite element codes, the global stiffness matrix is typically formed using the tangential stress–strain matrix. The elastic part of the latter, $\mathbf{D}_e$, defines the elastic stress–strain relations and is a function of the elastic tangential bulk modulus K and the shear modulus G. For critical state models, the bulk modulus K is often assumed to be a function of the effective mean stress p' according to

$$K = \frac{\partial p'}{\partial \varepsilon_v^e} = \frac{1+e}{\varkappa} p' = \frac{v p'}{\varkappa} \tag{5}$$

where ε_v^e denotes the elastic volumetric strain, e is the void ratio, $v = 1 + e$ is the specific volume, and $\varkappa$ is the slope of an unloading–reloading line in a $\ln p'$–v diagram. If Poisson's ratio μ is assumed to be constant, then the shear modulus G may be written as

$$G = \frac{3(1-2\mu)K}{2(1+\mu)} = \frac{3(1-2\mu)}{2(1+\mu)} \frac{v p'}{\varkappa} \tag{6}$$

Equations (5) and (6) show that the tangential bulk modulus K and the tangential shear modulus G become zero at zero effective mean stress. This can cause numerical problems in finite element calculations, but can be avoided by introducing a minimum effective mean stress, $p'_{\min}$, below which the bulk modulus and shear modulus are kept constant. A proper value for $p'_{\min}$ is problem specific and in this paper we set $p'_{\min} = 1\,\mathrm{kN/m^2}$.

In an explicit stress integration scheme, it is necessary to compute the intermediate stress state which lies on the yield surface if the stresses pass from an elastic state to a plastic state. This implies that the first task in the integration scheme is to determine if the given strain increment causes plastic yielding. If plastic yielding does occur, and the initial stress state is in the elastic region so that $f(\boldsymbol{\sigma}'_0, \varkappa_0) < 0$, then the second task is to find the stresses at the intersection point $\boldsymbol{\sigma}'_i$ so that $f(\boldsymbol{\sigma}'_i, \varkappa_0) = 0$. To determine if the given strain increment causes plastic yielding, an elastic trial stress needs to be computed. Since the elastic deformation is nonlinear for critical state models, using the initial tangential elastic modulus may lead to the wrong conclusion. This is shown in Fig. 1 where the elastic trial stress $\boldsymbol{\sigma}'_e$, based on the initial tangential modulus at $\boldsymbol{\sigma}'_0$, is inside the yield surface, but the true stress path passes from an elastic to a plastic state. To avoid this problem, a secant elastic bulk modulus can be used to compute the correct trial stress.

Integrating Eq. (5) for p' and ε_v^e gives the relationship $\Delta p' = p'(\exp((v/\varkappa)\Delta\varepsilon_v^e) - 1)$, where p' is the effective mean stress at $\boldsymbol{\sigma}'_0$. By definition, the secant elastic modulus $\bar{K}$ for a given elastic volumetric strain increment $\Delta\varepsilon_v^e$ is then

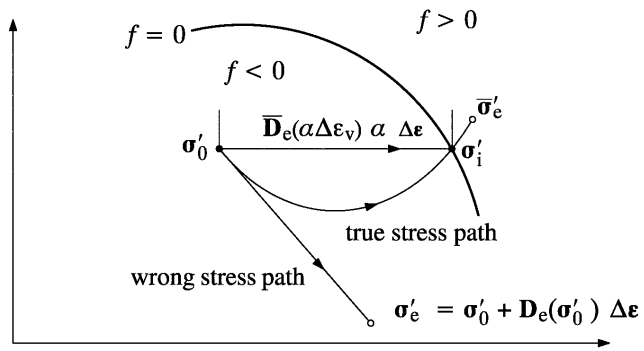

Fig. 1. Elastic trial stresses by tangential and secant elastic modulii

$$\bar{K} = \frac{\Delta p'}{\Delta\varepsilon_v^e} = \frac{p'}{\Delta\varepsilon_v^e}\left(\exp\left(\frac{v}{\varkappa}\Delta\varepsilon_v^e\right) - 1\right) \tag{7}$$

Note that at zero elastic volumetric strain, this secant elastic modulus approaches the tangential modulus defined by Eq. (5). Once $\bar{K}$ is known, the secant shear modulus $\bar{G}$ is defined by inserting Eq. (7) into Eq. (6).

For a given total strain increment $\Delta\boldsymbol{\varepsilon}$, it can initially be assumed that $\Delta\boldsymbol{\varepsilon}$ is purely elastic. This allows the secant elastic modulus $\bar{K}$ to be computed, using the total volumetric strain increment and the initial effective mean stress, which can then be used to find the correct elastic trial stress state. A simple procedure for determining if the given strain increment causes plastic yielding can now be summarised as follows:

1. Enter with a total strain increment $\Delta\boldsymbol{\varepsilon}$, an initial stress state $\boldsymbol{\sigma}'_0$, and an initial hardening parameter $\varkappa_0$.
2. Assume the strain increment is purely elastic and compute the secant elastic modulus $\bar{K}$ using (7) and the corresponding shear modulus $\bar{G}$.
3. Compute the secant elastic stiffness matrix $\bar{\mathbf{D}}_e$ based on $\bar{K}$ and $\bar{G}$.
4. Compute the elastic trial stress state $\bar{\boldsymbol{\sigma}}'_e$ according to
   $$\bar{\boldsymbol{\sigma}}'_e = \boldsymbol{\sigma}'_0 + \bar{\mathbf{D}}_e \Delta\boldsymbol{\varepsilon}\,.$$
5. If $f(\bar{\boldsymbol{\sigma}}'_e, \varkappa_0) \le 0$, the strain increment $\Delta\boldsymbol{\varepsilon}$ is purely elastic. Otherwise, plastic yielding takes place during the strain increment.

If the strain increment $\Delta\boldsymbol{\varepsilon}$ is found to cause an elastic transition, it is then necessary to locate the stresses, $\boldsymbol{\sigma}'_i$, at the intersection point with the yield surface. The problem of locating these stresses is equivalent to finding the scalar quantity α which satisfies the nonlinear equation

$$f(\boldsymbol{\sigma}'_i, \varkappa_0) = 0 \tag{8}$$

with

$$\boldsymbol{\sigma}'_i = \boldsymbol{\sigma}'_0 + \bar{\mathbf{D}}_e(\alpha\Delta\boldsymbol{\varepsilon}, \boldsymbol{\sigma}'_0)\alpha\Delta\boldsymbol{\varepsilon} \tag{9}$$

A zero value of α means that $\Delta\boldsymbol{\varepsilon}$ is purely plastic, while a value of 1 for α means that $\Delta\boldsymbol{\varepsilon}$ is entirely elastic. Thus, for an elastic to plastic transition, α is in the range $0 < \alpha < 1$.

Note that the elastic secant stiffness matrix in Eq. (9) is calculated using the initial stress state $\boldsymbol{\sigma}'_0$ and the elastic portion of the strain increment $\alpha\Delta\boldsymbol{\varepsilon}$. For a given strain increment and initial stress state, the elastic stress increment computed using a secant stiffness $\bar{\mathbf{D}}_e$ is exact, so that the intersection state $\boldsymbol{\sigma}'_i$ found from Eq. (8) is also exact. The nonlinear equation (8) can be solved using a variety of numerical methods such as the bisection, secant, Newton–Raphson and Regula–falsi techniques. The scheme used here, which is not well known, is the Pegasus method (Dowell and Jarratt [31]). This procedure converges very quickly, is unconditionally stable and does not need yield function gradients.

Once the intersection point $\boldsymbol{\sigma}'_i$ has been found, the standard elastoplastic stiffness matrix $\mathbf{D}_{ep}$ can be used to find the stress increment corresponding to the strain increment $(1-\alpha)\Delta\boldsymbol{\varepsilon}$.

Explicit stress integration with automatic substepping

In the modified Euler stress integration method (Abbo [28]), the strain increment is automatically subincremented using a local error estimate for the stresses and hardening parameter at each integration point. This error estimate is formed by taking the difference between a first order accurate Euler solution and a second order accurate modified Euler solution at each stage. Incorporating the features described above, this scheme can be summarised as follows:

1. Enter with the initial stress state $\boldsymbol{\sigma}'_0$, the initial hardening parameter $\varkappa_0$, the strain increment $\Delta\boldsymbol{\varepsilon}$.
2. Determine if the strain increment $\Delta\boldsymbol{\varepsilon}$ cases plastic yielding. If not, replace the stress state by the elastic trial stress state $\bar{\boldsymbol{\sigma}}'_e$, computed using the elastic modulii $\bar{K}$ and $\bar{G}$, and exit.
3. Find the intermediate stress state $\boldsymbol{\sigma}'_i$ on the current yield surface and the portion of the strain increment causing plastic deformation. Then set

   $$\boldsymbol{\sigma}'_0 = \boldsymbol{\sigma}'_i$$

   $$\Delta\boldsymbol{\varepsilon} = (1-\alpha)\Delta\boldsymbol{\varepsilon}$$

   The possibility of elastic unloading followed by plastic yielding should be taken into account in this step (see Abbo [28]).
4. Assume that all the strain increment $\Delta\boldsymbol{\varepsilon}$ is applied in one step.
5. Compute two sets of stress increments and hardening parameter increments using the Euler method and the modified Euler method, respectively.
6. Compute a relative error based on the difference of the two stress increments and the two hardening parameter increments.
7. If the error is larger than a prescribed tolerance, reduce the strain subincrement according to the error and the error tolerance and go to step 5 (see Abbo [28]).
8. If the error is smaller than a prescribed tolerance, update the stress state and the hardening parameter using the modified Euler solution. Compute the strain subincrement for the next step according to the error and the error tolerance.
9. If the updated stress state is outside the updated yield surface, project the stress state back to the yield surface using the drift correction method described by Potts and Gens [32].
10. Go to step 5 until the sum of the strain subincrements equals the total strain increment $\Delta\boldsymbol{\varepsilon}$.

Load stepping scheme for displacement elements

For uncoupled analysis, Abbo and Sloan [29] presented an incremental load stepping scheme with automatic step size control. The integration process selects each step so that the local error in the computed deflections is held below a prescribed value. The local error is measured by taking the difference between incremental solutions obtained from the first order accurate Euler scheme and the second order accurate modified Euler scheme. An unbalanced force correction is also included to prevent the accumulation of global errors. The scheme has proven to be particularly robust and permits a broad class of load-deformation paths to be integrated with only a small amount of drift from equilibrium. Since the method does not exploit any special features of the governing equations, it can be used to deal with a wide range of constitutive models.

Abbo and Sloan [29] and Abbo [28] demonstrated the effectiveness of their adaptive load stepping scheme by analysing several boundary value problems with simple elastoplastic models based on Mohr-Coulomb and Tresca yield functions. It was found that the error in the displacements can be controlled within an order of magnitude of the desired tolerance, independent of the number of coarse load increments supplied by the user. The speed of the automatic error control scheme compared favourably with the conventional forward Euler scheme. Indeed, the average CPU time per step for these two methods differed only marginally. The chief benefit of the automatic scheme is that it removes the guess work involved in specifying the load increments by hand. Moreover, it uses small load increments only where necessary.

The adaptive load stepping method of Abbo and Sloan [29] needs a minor modification in order to be used with critical state models. This is because, unlike simple Mohr-Coulomb or Tresca models, critical state models are nonlinear in the elastic range, and it is not possible to form the elastoplastic global stiffness matrix by subtracting the plastic stiffness terms from the elastic stiffness terms. Instead, the global stiffness matrix must be computed afresh at each step.

Time stepping scheme for mixed displacement–pore pressure elements

For coupled analysis of deformation and pore pressure, Sloan and Abbo [30] recently presented a new adaptive time stepping scheme. Using a similar philosophy to the load-stepping scheme described by Abbo and Sloan [29], the adaptive time stepping scheme attempts to choose the time subincrements so that, for a given mesh, the time-stepping error in the displacements is close to a specified tolerance. The local error in the displacements is found by taking the difference between the first order accurate backward Euler solution and the second order accurate Thomas and Gladwell solution [33]. Unlike existing

solution techniques, the new algorithm computes not only the displacements and pore pressures, but also their derivatives with respect to time.

The performance of this adaptive time stepping scheme has been demonstrated for simple elastoplastic models by Sloan and Abbo [34]. In all cases, the scheme was found to be able to constrain the global temporal error in the displacements to lie near the desired tolerance. It was proved that the behavior of the automatic procedure is largely insensitive to the size and distribution of the initial coarse time steps. In general, the performance of the automatic time stepping scheme compares favorably to that of the conventional backward Euler scheme. To achieve solutions of similar accuracy, the automatic and backward Euler schemes use a similar amount of computational effort. The backward Euler scheme is marginally faster for a crude analysis while the automatic scheme is much faster when an accurate solution is required. The chief advantage of the automatic method is that it removes the need to determine the time stepping error by an empirical trial and error procedure.

In this paper, the adaptive time stepping method of Sloan and Abbo [30] will be used to solve coupled displacement and pore pressure problems in soils whose behavior is simulated by critical state models. Due to the nonlinear behavior in the elastic part, both the elastic and plastic global stiffness matrices have to be reformed at each increment and in each iteration.

Critical state models implemented

The finite element code, SNAC, has been developed at the University of Newcastle over a number of years (see Abbo [28], Abbo and Sloan [29], and Sloan and Abbo [30]). Originally only conventional elastoplastic models, such as the Mohr-Coulomb, Tresca and Von Mises criteria were implemented, but now two critical state (CS) models have also been incorporated.

Generalized Cam-clay model

The first CS model is based on the modified Cam clay (MCC) yield function (2), and attempts to overcome a drawback of the MCC model which causes the failure stresses on the supercritical side to be overestimated. Assuming an associated flow rule, the proposed yield function and plastic potential take the following form:

$$f = g = \frac{1}{\beta^2}\left(\frac{(1+\beta')p'}{p'_0} - 1\right)^2 + \left(\frac{(1+\beta')q}{M(\theta)p'_0}\right)^2 - 1 \tag{10}$$

where β and β' are parameters that adjust the shape of the yield function and the plastic potential as shown in Fig. 2. Setting $\beta = \beta' = 1$ in (10) leads to the modified Cam-clay model. The parameter β is always set to 1 on the dry side of the critical state line and $\beta = \beta' \leq 1$ on the wet side of the critical state line.

In Eq. (10), the slope of the critical state line (CSL), M, is expressed as a function of the Lode angle θ, and determines the shape of the failure surface in the deviatoric plane (see Fig. 2). During the last two decades different functions have been proposed for modelling the failure surface in the deviatoric plane [5, 35–39]. One simple example, due to Gudehus [37], is

$$M = \frac{2\alpha M_{\max}}{1 + \alpha - (1-\alpha)\sin 3\theta} \tag{11}$$

where $M_{\max}$ is the slope of the CSL under triaxial compression ($\theta = 30°$). The parameter α can be set to

$$\alpha = \frac{3 - \sin\phi}{3 + \sin\phi} \tag{12}$$

in order to approximate a hexagonal Mohr-Coulomb failure surface. The parameter ϕ in Eq. (12) is the friction angel of the soil at critical state. One problem with the function (11) is that the resulting yield surface is convex only if $\alpha \geq 0.778$ (i.e. for a friction angle $\phi < 22°$). This is not appropriate for most soil types, and a better alternative to (11) is

$$M = M_{\max}\left(\frac{2\alpha^4}{1 + \alpha^4 - (1-\alpha^4)\sin 3\theta}\right)^{1/4} \tag{13}$$

By setting α according to Eq. (12), this yield surface coincides with the Mohr-Coulomb hexagon at all vertices in the deviatoric plane (see Fig. 2), while setting $\alpha = 1$ recovers the Von Mises circle. Note that this yield surface is differentiable for all stress states and is convex provided $\alpha \geq 0.6$ (i.e. for a friction angle $\phi \leq 48.59°$).

Unified clay and sand model

The second model implemented is the unified clay and sand model, CASM, developed by Yu [13]. CASM uses the

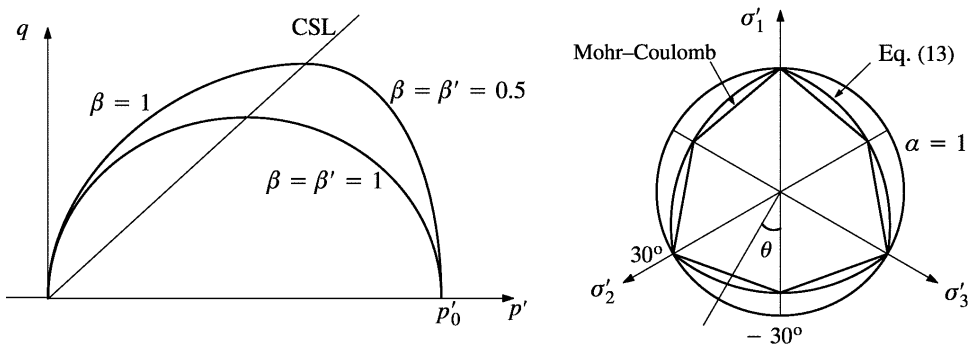

Fig. 2. Variation of the yield surface in the generalized version of the modified Cam-clay model

state parameter concept and a nonassociated flow rule with

$$f = \left(\frac{q}{Mp'}\right)^n + \frac{1}{\ln r} \ln \frac{p'}{p'_0} \tag{14}$$

where n is a parameter used to specify the shape of the yield function and r is a spacing ratio used to control the intersection point of the critical state line and the yield surface, as shown as Fig. 3. If n is set to 1 and r to the natural logarithmic base e in (14), the original Cam-clay yield function (1) is recovered. To approximate a Mohr-Coulomb hexagon, the same function as (13) can be used for the slope M of the CSL. It should be noted that the intersection point between the critical state line and the yield surface in this model does not necessarily occur at the maximum deviator stress (as in the original and modified Cam-clay models).

The plastic potential in CASM follows the stress–dilatancy relation of Rowe [40]

$$g = 3M \ln \frac{p'}{\zeta} + (3 + 2M) \ln\left(\frac{2q}{p'} + 3\right) - (3 - M) \ln\left(3 - \frac{q}{p'}\right) \tag{15}$$

where ζ is a size parameter (which is not used in the implementation of the model since only the derivatives of g are needed). Note that this plastic potential can also be used in conjunction with the yield function (10) to give yet another nonassociated critical state model.

The elastic part of these two critical state models is the same as discussed earlier, with the tangential bulk modulus being defined by Eq. (5) and the shear modulus by (6). They both assume a constant Poisson's ratio and their hardening laws are also identical. The yield surface size (isotropic preconsolidation pressure) p'_0 is taken as the hardening parameter and is related to the plastic volumetric strain ε_v^p by the equation

$$\delta p'_0 = \frac{v p'_0}{\lambda - \varkappa} \delta \varepsilon_v^p \tag{16}$$

where λ is the slope of the normal compression line in a $\ln p'$–v diagram.

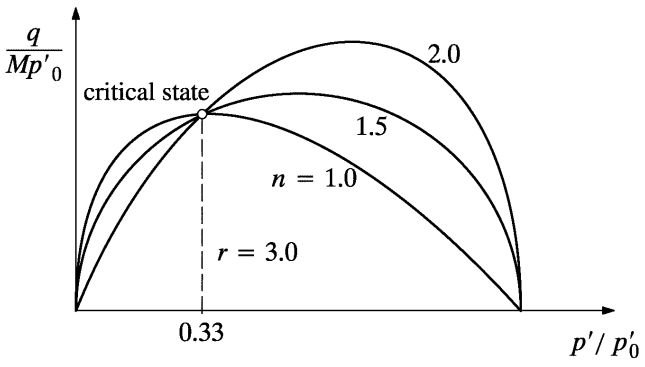

Fig. 3. Variation of the yield surface in the unified model for clay and sand (CASM) by Yu [13]

Verification and application

In this section, the critical state models described above are used to analyse several practical problems. In all calculations, the constitutive laws are integrated accurately using a relative local error tolerance of 10^{-6} for the stresses, in conjunction with an absolute tolerance of 10^{-9} for drift from the yield surface (see Abbo [28]). In the analyses with the automatic load or time stepping schemes, a relative displacement error tolerance of 10^{-4} is used (see Abbo and Sloan [29], and Sloan and Abbo [30]). In the uncoupled analyses of triaxial tests using the Newton–Raphson scheme, a relative error tolerance of 10^{-6} for the unbalanced forces is used.

Triaxial tests

Numerical simulation of triaxial compression tests is one way to verify the implementation of a critical state model. In an ideal triaxial test, the stresses and strains are uniform and thus the computed stresses and strains at each integration point should follow the constitutive relations exactly. To verify this, the modified Cam-clay model is chosen and the following material properties are used

$$M = 1.2, \quad \lambda = 0.2, \quad \varkappa = 0.02, \quad \mu = 0.3$$
$$p'_0 = 60, \quad k = 10^{-8}$$

where the parameter k is the permeability. The units of the properties are not important as long as they are used in a consistent manner. A quarter of the cylindrical specimen of 0.5 unit in diameter and 1.0 unit in length is discretized into eight triangular 6-noded elements. Two types of initial conditions are considered, which respectively represent a lightly overconsolidated clay with an overconsolidation ratio of 1.2 (designated as normally consolidated NCC) and a heavily overconsolidated clay with an overconsolidation ratio of 6 (designated as OCC):

$$\text{Initial condition of NCC}: \sigma'_{r0} = \sigma'_{a0} = 50, \quad e_0 = 1.50$$
$$\text{Initial condition of OCC}: \sigma'_{r0} = \sigma'_{a0} = 10, \quad e_0 = 1.53$$

In the above σ'_{r0} and σ'_{a0} denote the initial radial and axial stresses respectively, and e_0 is the initial void ratio. The radial stress is kept constant while a prescribed axial strain is imposed, as in a conventional triaxial compression test.

Three different analyses are carried out here: an uncoupled elastoplastic analysis with no pore pressure, a coupled analysis of drained compression (with drainage at ends of the specimen), and a coupled analysis of undrained compression. The first two analyses should produce the same results if the applied strain rate in the coupled analysis is sufficiently small with respect to the permeability. For the uncoupled elastoplastic analysis and coupled drained analysis, an axial strain of 50% is imposed in 50 coarse increments. For the coupled undrained analysis, an axial strain of 5% is first applied in 50 increments and an additional 45% in another 50 increments. The time step for the coupled analysis is set to 10^8 which guarantees no excess pore pressure in the drained specimen and a uniform excess pore pressure in the undrained specimen.

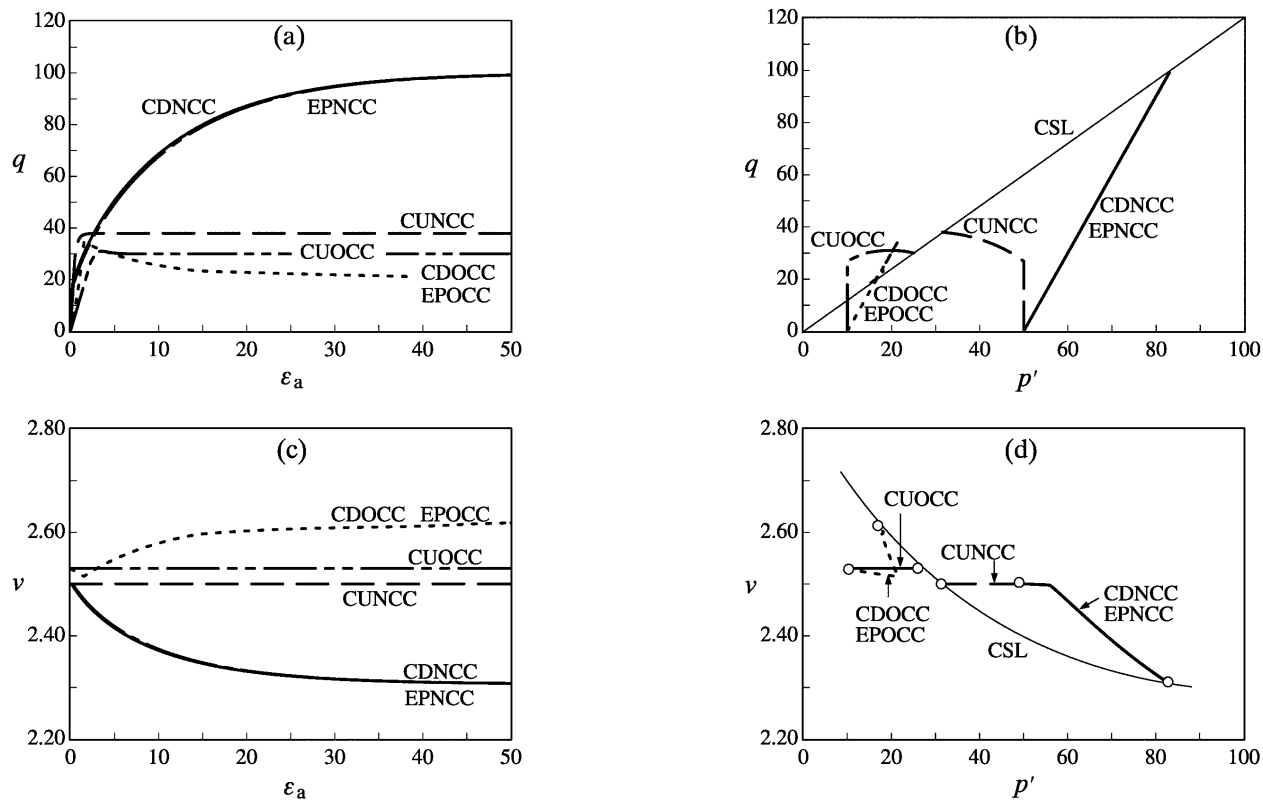

Fig. 4. Simulated results for triaxial tests; **a** Axial strain vs. deviator stress; **b** Effective mean stress vs. deviator stress; **c** Axial strain vs. specific volume; **d** Effective mean stress vs. specific volume. (EP: uncoupled elastoplastic analysis, CD: coupled drained analysis, CU: coupled undrained analysis, NCC: lightly overconsolidated clay, OCC: heavily overconsolidated clay)

The simulated results are shown in Fig. 4. As expected, the uncoupled elastoplastic analysis and coupled drained analysis produce almost identical results. Hardening of the lightly overconsolidated soil and softening of the heavily overconsolidated soil are well captured. At the end of the applied axial strain, the soil reaches the critical state line under all the test conditions. For the uncoupled analysis and coupled drained analysis of the lightly overconsolidated clay (EPNCC and CDNCC in Fig. 4), an axial strain of 50% is needed before the critical state is reached and the stress path follows the 1:3 line in the p'–q diagram. For the uncoupled analysis and coupled drained analysis of the heavily overconsolidated clay (EPOCC and CDOCC in Fig. 4), the critical state is reached at about 20% of axial strain and the stress path first intersects the initial yield surface and then moves back to the critical state line. For the coupled undrained analyses of both the lightly and heavily overconsolidated clay, the critical state is reached with an axial strain less than 3%. The stress path for the CUNCC analysis approaches the critical state line from the wet side, while the stress path for the CUOCC analysis approaches the critical state line from the dry side.

For this simple example, other stress integration and load and time stepping methods may produce similar results if sufficient increments are used. For example, if the same amount of axial strain is applied in 50 increments using the standard Newton–Raphson method, the results obtained are very similar to those shown in Fig. 4. However, the total CPU time required for the automatic load stepping scheme is roughly one third of that for the standard Newton–Raphson method, even though the number of load subincrements required in the former is larger than the number of iterations in the latter (see Figs. 5 and 6). In the automatic scheme, a pronounced increase in the number of load subincrements can be observed whenever the soil yield or softens or reaches the critical state line. The number of iterations for the Newton–Raphson method, on the other hand, is more or less

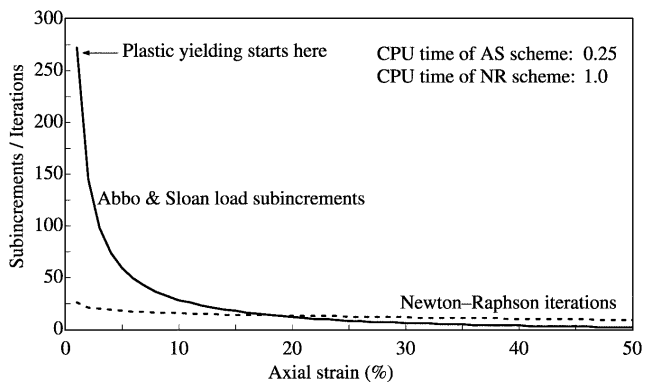

Fig. 5. Number of load subincrements in the Abbo and Sloan scheme and number of iterations in the Newton–Raphson scheme for uncoupled analysis of the lightly overconsolidated clay (NCC)

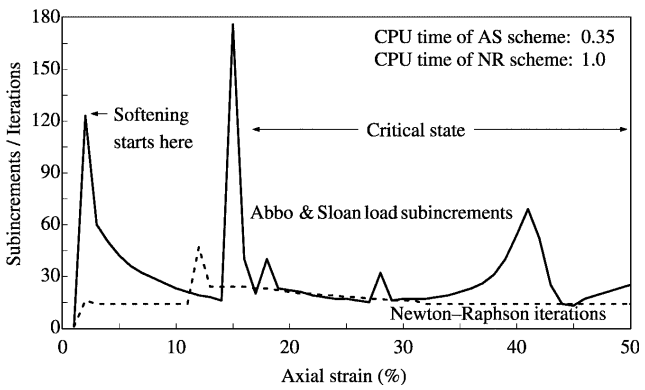

Fig. 6. Number of load subincrements in the Abbo and Sloan scheme and number of iterations in the Newton–Raphson scheme for uncoupled analysis of the heavily overconsolidated clay (OCC)

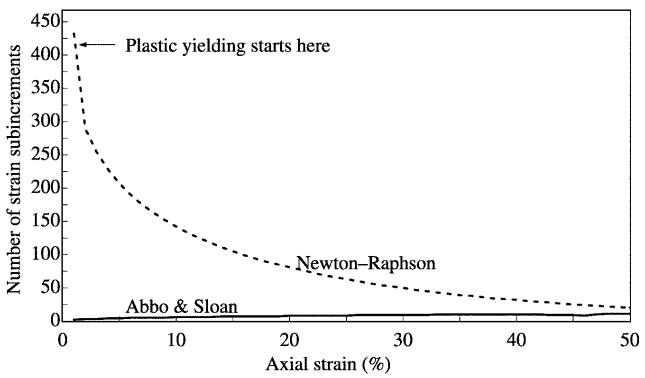

Fig. 7. Average number of strain subincrements in stress integration for uncoupled analysis of the lightly overconsolidated clay (NCC)

constant over the entire range of axial strain. Another interesting quantity is the average number of strain subincrements required by the automatic stress integration procedure at each Gauss point. The Newton–Raphson method, with 50 increments of fixed size, requires a significantly larger number of strain subincrements than Abbo and Sloan's automatic method (see Figs. 7 and 8). That is why the Newton–Raphson method requires a larger total CPU time.

Undrained cylindrical cavity expansion

Analytical solutions for undrained expansion of cylindrical and spherical cavities in soils modelled by original and modified Cam clay have been derived by Collins and Yu [41]. These results provide another valuable benchmark for verifying finite element predictions. In this paper, the analytical results for undrained expansion of a cylindrical cavity are used to check the finite element solutions from the modified and original Cam-clay models.

The analytical solutions obtained by Collins and Yu [41] are for cavity expansion in an infinite soil medium. In the finite element analysis, a finite outer radius, equal to 20 times the initial cavity radius, is used (see Fig. 9). A sensitivity analysis suggested that, for the soil properties used in our calculations, this geometry is sufficient to simulate

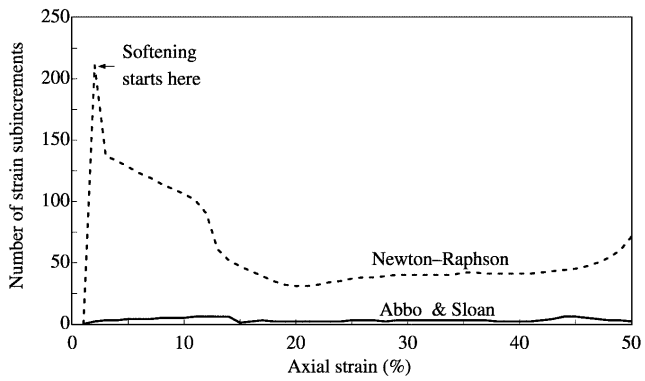

Fig. 8. Average number of strain subincrements in stress integration for uncoupled analysis of the heavily overconsolidated clay (OCC)

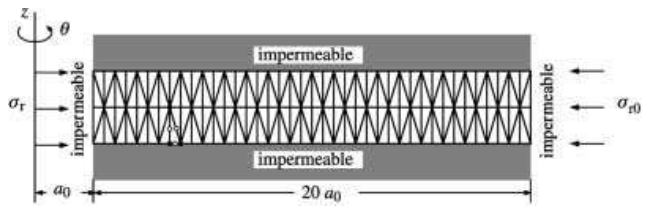

Fig. 9. Finite element representation of undrained cylindrical cavity expansion

the behavior of cavity expansion in an infinite clay soil. In the analysis, the total radial pressure at the boundary of the cylinder is kept constant while the total radial pressure at the cavity wall is increased until the cavity is expanded by 50% (to a radius of 1.5). This amount of displacement is imposed over 100 increments. All boundaries are sealed for drainage. The element used is the triangular 6-noded element with pore pressure freedoms at its three corner nodes.

The soil parameters used for modified Cam clay are those relevant to London clay,

$$M = 0.888,\ \lambda = 0.161,\ \varkappa = 0.062,\ \mu = 0.3\ \ \Gamma = 2.759$$

where Γ is the specific volume at unit p' on the critical state line in a v–ln p' diagram. The initial void ratio and the overconsolidation ratio are taken as

$$e_0 = 1.0 \quad \mathrm{OCR} = 1$$

For modified Cam clay, the specific volume N at unit p' on the normal compression line is

$$N = \Gamma + (\lambda - \varkappa)\ln\ 2 = 2.828$$

which gives the initial preconsolidation pressure p'_0 as

$$p'_0 = \exp((N - e_0 - 1)/\lambda) = 170.8$$

Assuming the initial stress state is isotropic and OCR = 1, the initial stresses are then

$$\sigma'_{z0} = \sigma'_{r0} = \sigma'_{\theta 0} = 170.8$$

The stresses in the analytical solutions of Collins and Yu are all normalised by the undrained shear strength, which is given by

$$S_u = 0.5\,M\,\exp((\Gamma - e_0 - 1)/\lambda) = 49.52$$

The soil parameters used for original Cam clay are the same as those for modified Cam clay, except that the specific volume N becomes

$$N = \Gamma + (\lambda - \varkappa) = 2.858$$

Therefore, the initial preconsolidation pressure p'_0 is

$$p'_0 = \exp((N - e_0 - 1)/\lambda) = 206.3$$

which is also the isotropic initial stress for OCR = 1.

Another key soil parameter is the permeability. It is often perceived that under undrained conditions the permeability does not play any role in the determination of effective stresses or excess pore pressures. This is true only when the undrained condition of zero volume change is satisfied at all local points. In a finite element analysis, however, the condition of zero volume change is enforced only in a global, and not a local, sense. Due to local drainage, a large permeability (compared to the loading rate) will smooth any gradients in the excess pore pressures and eventually result in a uniform distribution of excess pore pressure. In order to guarantee that the undrained condition is satisfied both globally and locally, a very fast loading rate is required. In the undrained cavity expansion analyses, the permeability of the soil is set to 10^{-9} and the prescribed radial displacement of 0.5 is applied over a time period of 100 units. Test runs showed that decreasing the permeability further, or making the loading rate larger, would not lead to any change of excess pore pressure.

The numerical and analytical cavity expansions curves for the modified Cam clay analyses are shown in Fig. 10. The total radial stress and excess pore pressure predictions at the cavity wall compare well with the analytical values. It is interesting to note that the difference between the total radial stress and the excess pore pressure, i.e. the effective radial stress at the cavity wall, becomes constant after a certain deformation. This situation arises once the stresses at the cavity wall reach the critical state.

The distribution of the effective stresses and excess pore pressure at the maximum cavity expansion are shown in Fig. 11. Near the cavity wall, both the analytical and numerical effective stresses remain largely unchanged and the soil is at the critical state. Away from the wall, the effective radial stress exhibits a peak value at about

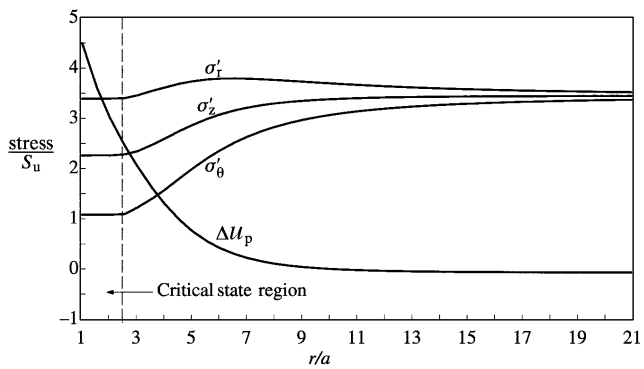

Fig. 11. Distribution of effective stresses and excess pore pressure in cavity of modified Cam clay

$r/a = 6.0$ and the effective axial and circumferential stresses increase gradually to their initial values.

The total and effective stress paths in p'–q space for this problem are plotted in Fig. 12. The total and effective stress paths at different radial locations follow basically the same curves, but end at different positions. The effective stress path hits the critical state line at $q = 2S_u$. Once the critical state is reached, the effective stress path remains stationary and the total stress path moves parallel to the mean stress axis, which implies that any further increase in the total mean stress is completely balanced by a corresponding increase in the excess pore pressure.

The results obtained for the original Cam-clay model are illustrated in Figs. 13–15. The total radial stresses and excess pore pressures at the cavity wall, shown in Fig. 13, are close to those observed for modified Cam clay, even though different initial stresses are used in the two models. Also, the effective stress path intersects the critical state line at almost the same point in the p'–q diagram as in the modified Cam clay analyses (Fig. 15). The critical state zone developed around the cavity wall, however, is slightly smaller than that in modified Cam clay and, as shown in Fig. 14, the effective radial stress does not exhibit a distinct peak outside the critical state region.

Uncoupled analysis of rigid strip footing

The collapse of a rigid strip footing is a well-known problem for testing stress integration and load stepping

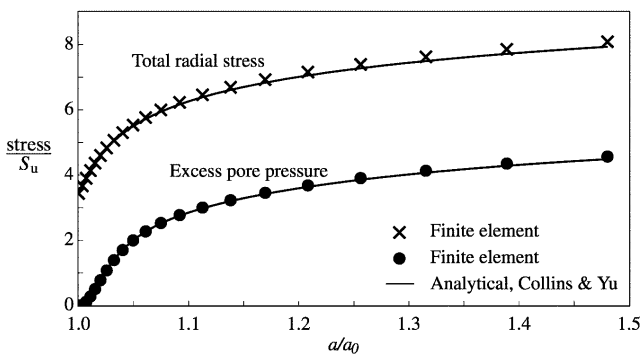

Fig. 10. Total radial stress and excess pore pressure at the cavity wall in modified Cam clay

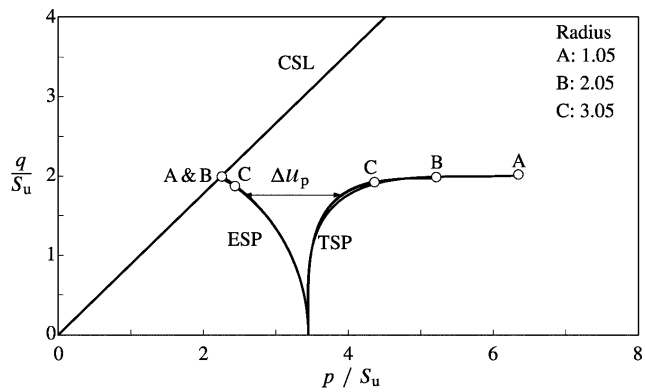

Fig. 12. Effective and total stress paths during cavity expansion in modified Cam-clay

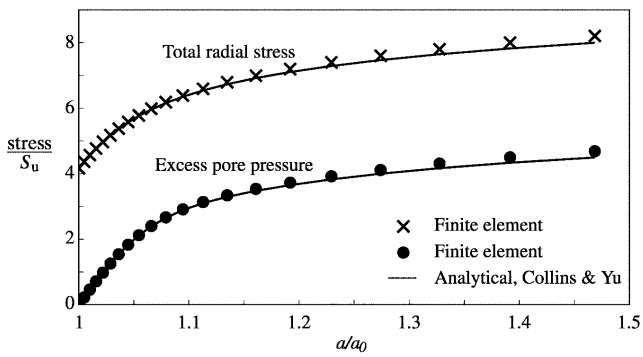

Fig. 13. Total radial stress and excess pore pressure at the cavity wall in original Cam clay

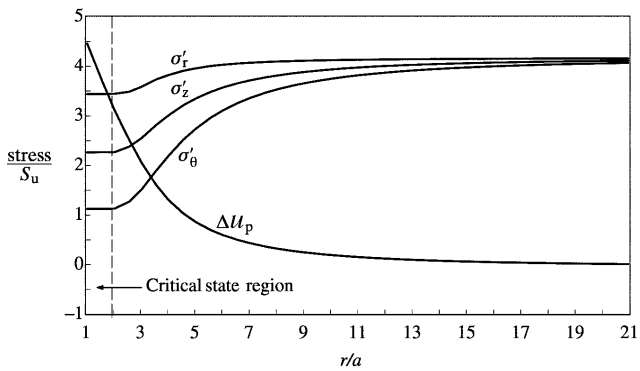

Fig. 14. Distribution of effective stresses and excess pore pressure in cavity of original Cam clay

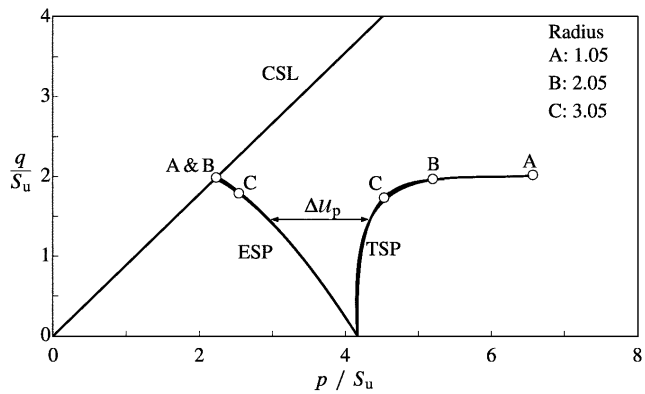

Fig. 15. Effective and total stress paths during cavity expansion in original Cam clay

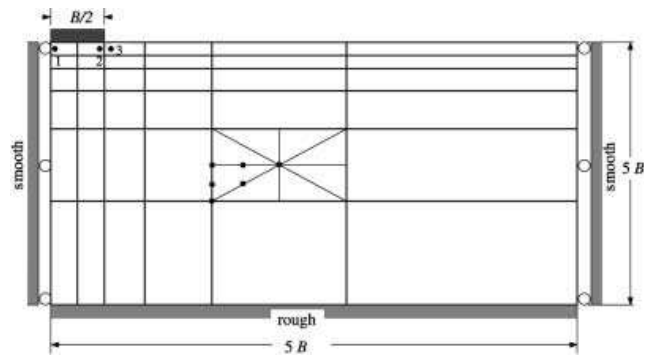

Fig. 16. Mesh for footing analysis with 625 nodes, 288 elements and 1143 degrees of freedom (points 1, 2 and 3 are used for stress path study)

methods. Due to the singularity at the edge of the footing and the strong rotation of the principal stresses, this case has proved to be difficult for standard critical state analyses with Newton–Raphson and modified Newton–Raphson iteration methods (see Gens and Potts [19]).

Two constitutive models are used to simulate the subgrade soils, namely the modified Cam-clay model (MCC) and the generalized Cam-clay model (GCC). For the MCC model, the material parameters are assumed to be:

$$M = 0.898, \quad \lambda = 0.25, \quad \varkappa = 0.05, \quad \mu = 0.3,$$
$$\gamma = 6\,\mathrm{kN/m^3}$$

Since the density used to generate the geostatic initial stress corresponds to the submerged density of the soil, the results from this uncoupled analysis will be comparable to those from a coupled analysis to be considered later. The critical state void ratio at $p' = 1$ is assumed to have a homogenous value of 1.6 and the soil is assumed to be overconsolidated to 50 kPa at the ground surface.

The material parameters for the GCC model are the same as those for the MCC model, with α (in Eq. (12)) being set to 0.77 to approximate the Mohr-Coulomb failure surface in the deviatoric plane. The parameter β' is set to 0.5.

The footing geometry and the element mesh are shown in Fig. 16. The half width of the footing $B/2$ is set to 1 unit, and the domain of 10×10 units is divided into 288 triangular 6-noded elements with a total of 1143 degrees of freedom. The left and right boundaries are fixed in the horizontal direction but allowed to move in the vertical direction, while the bottom boundary is locked in both directions. A prescribed displacement of $0.2B$ is applied to the footing in 50 coarse increments, and an equivalent footing load is found by summing the appropriate nodal reactions.

The computed load–displacement curves for both soil models are shown in Fig. 17. For the MCC model, no obvious collapse load can be seen under an applied displacement equal to 20% of the footing width. The footing loads computed for the GCC model are slightly higher than those for the MCC model, probably due to the use of $\beta' = 0.5$, and asymptote toward a limiting value of 47 units at the end of the applied displacement.

The stress paths at points underneath the footing are shown in Fig. 18 for the MCC model. The stress paths for points 2 and 3 first reach the supercritical side of the initial yield surface and then gradually yield towards the CSL, while the stress path at point 1 first moves along the CSL, intersects the initial yield surface and then moves horizontally across the CSL. Note that all stress paths reach the critical state line at least once or twice, but none remain stationary.

Unlike the MCC model, the critical state line for the GCC model is not unique in the p–q diagram. Indeed, any line between the two CSLs shown in Fig. 19 can be a failure

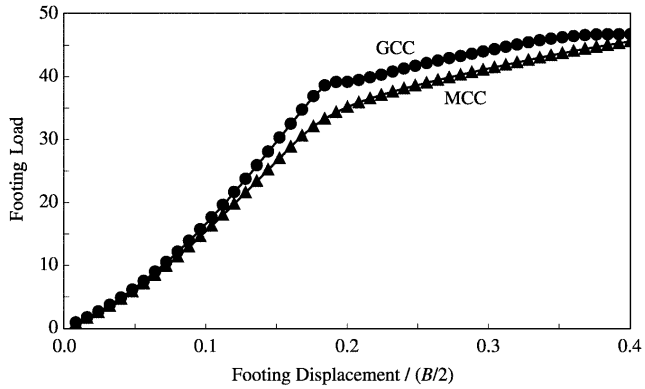

Fig. 17. Footing load versus footing displacement for uncoupled analysis of modified Cam clay (MCC) and generalised Cam clay (GCC)

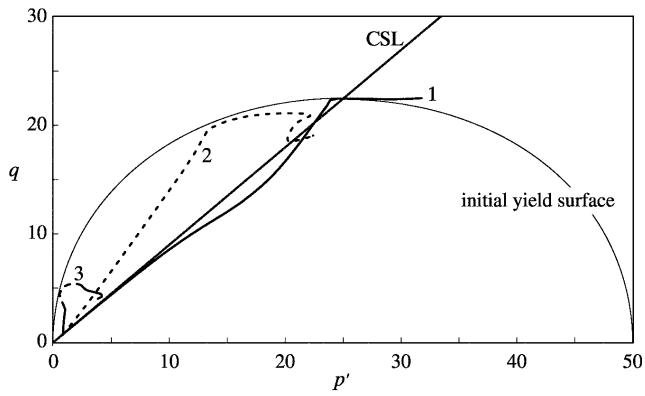

Fig. 18. Stress paths at different points underneath footing for uncoupled analysis with modified Cam clay (MCC)

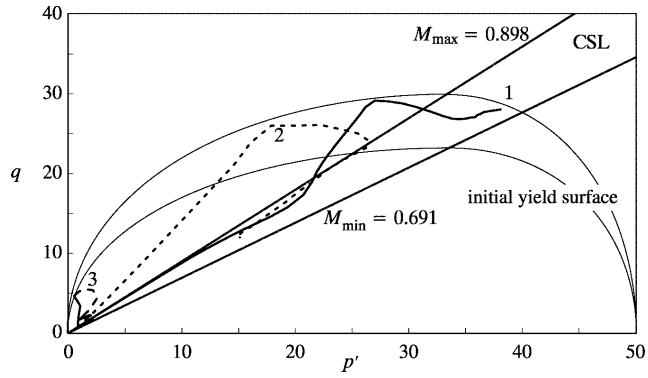

Fig. 19. Stress paths at different points underneath footing for uncoupled analysis with generalised Cam clay (GCC)

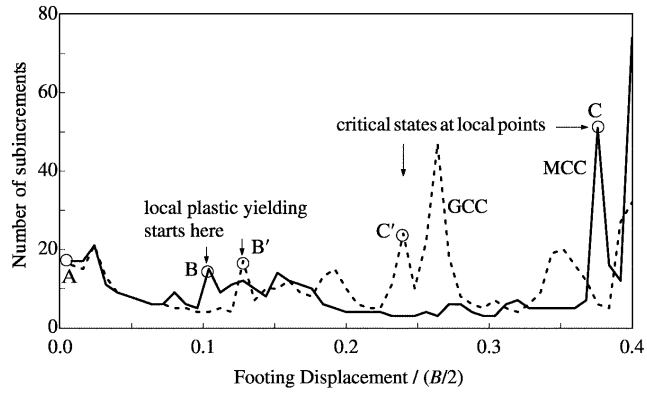

Fig. 20. Number of load subincrements versus footing displacement for the modified Cam clay (MCC) and generalised Cam clay (GCC) analyses

line, depending on the orientation and relative values of the principal stresses. The maximum slope M_{max} of the CSL corresponds to failure in triaxial compression (at a Lode angle $\theta = 30°$), while the minimum slope M_{min} corresponds to failure under triaxial extension ($\theta = -30°$). In Fig. 19, all stress paths end between the two CSLs. The stress paths for points 2 and 3 end closer to the CSL of slope M_{max}, while the stress path at point 1 ends closer to the CSL of slope M_{min}.

The number of subincrements in each coarse increment of prescribed displacement are plotted in Fig. 20. Comparing this plot with Figs. 17–19, we see that the number of subincrements increases at turning points in the material nonlinearity. At the start of loading (point A), a relatively large number of subincrements are needed, due to the strongly nonlinear elastic behaviour. The number of subincrements then decreases until local plastic yielding starts at point B for the MCC model and B′ for the GCC model. When failure is reached at points within the grid (C and C′), the number of subincrements increases significantly. These results indicate that, without the automatic stepping method, it should be very difficult to select the correct load increments to reflect the material nonlinearity. Figure 20 reveals that local failure starts earlier in the GCC model (point C′) than in the MCC model (point C), which is consistent with the shapes of the two failure surfaces in the deviatoric plane.

Coupled analysis of rigid strip footing

The rigid footing problem discussed in the previous subsection is now studied using a fully coupled analysis. The boundaries in Fig. 16 are all undrained except the top one. The same amount of footing displacement is applied in 100 equal increments, but is applied over different time periods which correspond to drained, partially drained, and undrained conditions. The drained condition corresponds to a very slow loading rate where no excess pore pressure is generated. The results obtained from such an analysis should theoretically be identical to those from the uncoupled analysis in the previous subsection.

The same soil parameters used in the uncoupled analysis are used here. One additional parameter needed for the coupled analysis is the permeability, which is set to 10^{-8}. The loading rate for the problem is defined as

$$\omega = \frac{\Delta w/t}{k\gamma_w} \tag{17}$$

where Δw is the equivalent footing pressure applied over the time period t, k is the permeability and γ_w is the unit weight of water. If ω is very small, the soil effectively

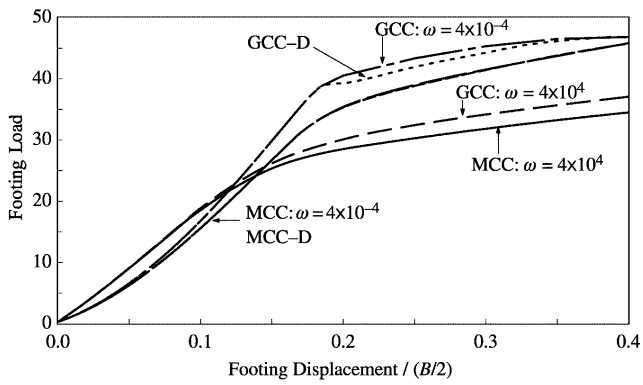

Fig. 21. Footing loads under different loading rates for coupled analyses of modified Cam clay (MCC) and generalised Cam clay (GCC). The results from the uncoupled analysis are marked as MCC–D and GCC–D

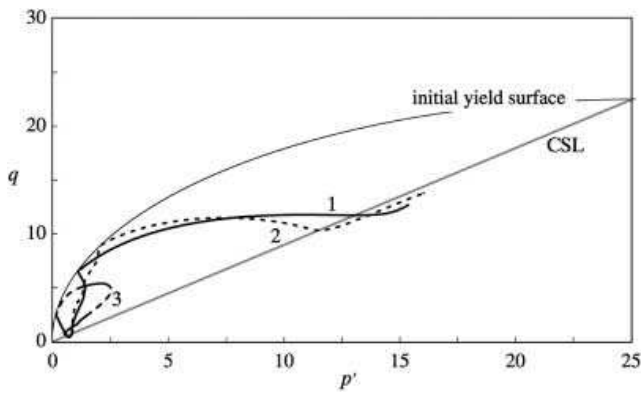

Fig. 22. Stress paths at different points underneath footing for coupled analysis with modified Cam clay and $\omega = 4 \times 10^4$

behaves under drained conditions. As ω increases, the behaviour of the soil changes from drained to undrained.

The load–displacement curves for the coupled analyses are shown in Fig. 21. For the MCC model, the results from the coupled analysis with a loading rate $\omega = 4 \times 10^{-4}$ are almost identical to the drained results (MCC–D) from the uncoupled analysis. For the GCC model, the load-displacement curve from the coupled analysis with a loading rate $\omega = 4 \times 10^{-4}$ is slightly smoother than the drained curve (GCC–D) from the uncoupled analysis. In general, as the loading rate increases, the computed footing load increases at small displacements but decreases at large displacements.

Figure 22 shows three stress paths for the MCC model with a fast loading rate $\omega = 4 \times 10^4$. In this case, the soil behaves essentially in an undrained manner. It can be noted that initial plastic yielding takes place at a much lower effective mean stress than in the completely drained case of Fig. 18. It can also be seen that the soil at points 1 and 2 is close to the undrained condition and the soil at point 3 deforms in a partially drained condition. The stress paths for the GCC model with the loading rate $\omega = 4 \times 10^4$ are shown in Fig. 23 and are similar to those in Fig. 22 for the MCC model. Compared with the completely drained

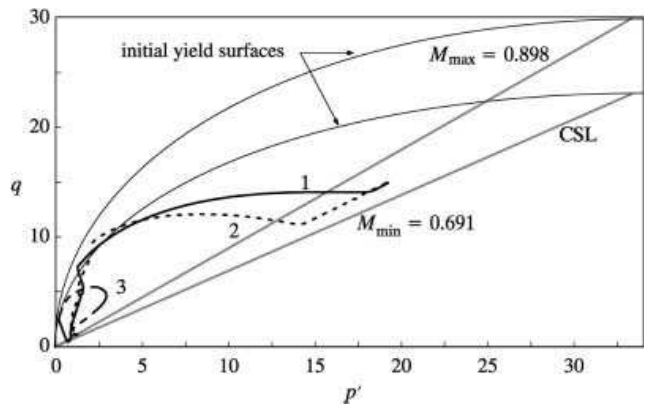

Fig. 23. Stress paths at different points underneath footing for coupled analysis with generalised Cam clay and $\omega = 4 \times 10^4$

case of Fig. 19, the initial yielding at all 3 points takes place at lower effective mean stresses and are closer to the minimum initial yield surface. At the end of the prescribed displacement, all stress paths finish between the two CSLs.

Conclusions

In this paper, a number of automatic solution schemes have been tested with two types of critical state models. The modified Euler method, described in Abbo [28], has proved to be an efficient and reliable stress integration procedure. This confirms the general findings of Gens and Potts [19] who concluded that explicit subincrementation techniques work well for complex soil models. For uncoupled problems, the automatic load incrementation algorithm of Abbo and Sloan [29] provided a simple and robust method for performing accurate nonlinear finite element analysis. Similarly, the automatic time stepping scheme of Sloan and Abbo [30] gave good results for coupled analysis of a variety of triaxial test cases and the undrained cavity expansion case. No numerical problems were encountered with any of the automatic schemes used in the calculations and this would be a major attraction for large scale, practical computations.

As expected, the number of substeps in the automatic load–displacement integration was found to be highly sensitive to the specific nature of the constitutive law used. Without an automatic scheme it would be difficult to determine a suitable series of load increments, even for a simple problem.

References

1. **Roscoe KH, Schofield AN, Wroth CP** (1958) On the yielding of soils. Geotechnique 8: 22–52
2. **Roscoe KH, Schofield AN** (1963) Mechanical behaviour of an idealised "wet" clay'. Proceeding of 2nd European Conference on Soil Mechanics & Foundation Engineering, Wiesbaden 1: 47–54
3. **Schofield AN, Wroth CP** (1968) Critical State Soil Mechanics, McGraw-Hill, London
4. **Roscoe KH, Burland JB** (1968) On the generalised stress–strain behaviour of "wet" clay. Engineering Plasticity, Cambridge University Press, pp. 535–560
5. **Zienkiewicz OC, Humpheson C, Lewis RW** (1975) Associated and non-associated visco-plasticity and plasticity in soil mechanics. Geotechnique. 25: 671–689

6. **Zienkiewicz OC, Naylor DJ** (1973) Finite element studies of soils and porous media. In: Oden JT, de Arantes ER (Eds.) Lecturer Finite Elements in Continuum Mechanics, UAH Press, pp. 459–493
7. **Ohta H, Wroth CP** (1976) Anisotropy and stress reorientation in clay under load. Proceeding of 2nd International Conference on Numerical Methods in Geomechanics, Blacksburg 1: 319–328
8. **Runesson K, Axelsson K** (1977) An initially anisotropic yield criterion for clays. In: Bergan P, et al. (Eds.) Proceeding of International Conference on Finite Elements in Nonlinear Solid and Structural Mechanics, Tapir, Trondheim, pp. 513–533
9. **Nova R, Wood DM** (1979) A constitutive model for sand in triaxial compression. Int. J. Num. Anal. Meth. Geomech. 3: 255–278
10. **Carter JP, Booker JR, Wroth CP** (1982) A critical state model for cyclic loading. In: Pande GN, Zienkiewicz OC (Eds.) Soil Mechanics – Transient and Cyclic Loads, Wiley, Chichester, pp. 219–252
11. **Naylor, DJ** (1985) A continuous plasticity version of the critical state model. Int. J. Num. Meth. Eng. 21: 1187–1204
12. **Crouch RS, Wolf JP, Dafalias YF** (1994) Unified critical state bounding surface plasticity model for soil. J. Eng. Mech. ASCE 120(11): 2251–2270
13. **Yu HS** (1998) CASM: A unified state parameter model for clay and sand. Int. J. Num. Anal. Meth. Geomech. 22: 621–653
14. **Smith IM** (1970) Incremental numerical analysis of simple deformation problem in soil mechanics. Geotechnique 20: 357–372
15. **Naylor DJ** (1975) Non-linear finite elements for soils, PhD Thesis, University of Swansea
16. **Simpson B** (1973) Finite element computations in soil mechanics, PhD Thesis, University of Cambridge
17. **Carter JP, Randolph MF, Wroth CP** (1979) Stress and pore pressure changes in clay during and after the expansion of a cylindrical cavity. Int. J. Num. Anal. Meth. Geomech. 3: 305–322
18. **Britto AM, Gunn MJ** (1987) Critical State Soil Mechanics via Finite Elements, Ellis Horwood, Chichester
19. **Gens A, Potts DM** (1988) Critical state models in computational geomechanics. Eng. Comput. 5: 178–197
20. **Simo JC, Taylor RL** (1985) Consistent tangent operators for rate-independent elasto-plasticity. Comp. Meth. Appl. Mech. Eng. 48: 101–118
21. **Oritz M, Simo JC** (1986) An analysis of a new class of integration algorithms for elasto-plastic constitutive relations. Int. J. Num. Meth. Eng. 23: 353–366
22. **Borja RI** (1991) Cam–Clay plasticity, Part II: Implicit integration of constitutive equations based on a non-linear elastic stress predictor. Comp. Meth. Appl. Mech. Eng. 88: 225–240
23. **Potts DM, Ganendra D** (1992) A comparison of solution strategies for non-linear finite element analysis of geotechnical problems. Proceedings of 3rd International Conference on Computational Plasticity, Barcelona, pp. 803–814
24. **Potts DM, Ganendra D** (1994) An evaluation of substepping and implicit stress point algorithms. Comp. Meth. Appl. Mech. Eng. 119: 341–354
25. **Booker JR, Small JC** (1975) An investigation of the stability of numerical solutions of Biot's equations of consolidation. Int. J. Solids and Struct. 11: 907–917
26. **Vermeer PA, Verruijt A** (1981) An accuracy condition for consolidation by finite elements. Int. J. Num. Anal. Meth. Geomech. 5: 1–14
27. **Sloan SW** (1987) Substepping schemes for the numerical integration of elastoplastic stress–strain relations. Int. J. Num. Meth. Eng. 24: 893–911
28. **Abbo AJ** (1997) Finite Element Algorithms for Elastoplasticity and Consolidation, PhD Thesis, the University of Newcastle
29. **Abbo AJ, Sloan SW** (1996) An automatic load stepping algorithm with error control. Int. J. Num. Meth. Eng. 39: 1737–1759
30. **Sloan SW, Abbo AJ** (1999) Biot consolidation analysis with automatic time stepping and error control. Part 1: Theory and implementation. Int. J. Num. Anal. Meth. Geomech. 23: 467–492
31. **Dowell M, Jaratt P** (1972) The "Pegasus" method for computing the root of an equation. BIT 12: 503–508
32. **Potts DM, Gens A** (1985) A critical assessment of methods of correcting for drift from the yield surface in elastoplastic finite element analysis. Int. J. Num. Anal. Meth. Geomech. 9: 149–159
33. **Thomas RM, Gladwell I** (1988) Variable-order variable step algorithm for second-order systems. Part 1: The methods'. Int. J. Num. Meth. Eng. 26: 39–53
34. **Sloan SW, Abbo AJ** (1999) Biot consolidation analysis with automatic time stepping and error control. Part 2: Applications. Int. J. Num. Anal. Meth. Geomech. 23: 493–529
35. **Matsuoka H, Nakai T** (1974) Stress deformation and strength characteristics of soil under three different principal stresses. Proceeding of Japanese Society of Civil Engineering 232: 59–70
36. **Lade PV, Duncan JM** (1975) Elastoplastic stress–strain theory for cohesionless soil. J. Geotech. Eng. Div. ASCE 101: 1037–1053
37. **Zienkiewicz OC, Pande GN** (1977) Some useful forms of isotropic yield surfaces for soil and rock mechanics. In: Gudehus G (Ed.) Finite Elements in Geomechanics, Chapter 5, pp. 179–198
38. **Van Eekelen HAM** (1980) Isotropic yield surfaces in three dimensions for use in soil mechanics. Int. J. Num. Anal. Meth. Geomech. 4: 89–101
39. **Randolph MF** (1982) Generalising the Cam-clay models. Workshop on Implementation of Critical State Soil Mechanics in Finite Element Computation, Cambridge
40. **Rowe PW** (1962) The stress–dilatancy relation for static equilibrium of an assembly of particles in contact. Proceedings of Royal Society A267: 500–527
41. **Collins IF, Yu HS** (1996) Undrained cavity expansions in critical soils. Int. J. Num. Anal. Meth. Geomech. 20: 489–516